PCCP

ROYAL SOCIETY OF CHEMISTRY

PAPER

View Article Online
View Journal | View Issue

Check for updates

Cite this: *Phys. Chem. Chem. Phys.*, 2025, **27**, 24569

Stability and comparative analysis of two-dimensional AN_3 (A = Si, Sn) monolayers as hosts for K-ion storage: insights from first-principles calculations

Liaqat Ali and Chong-Wen Zhou *

Received 3rd September 2025,
Accepted 20th October 2025

DOI: 10.1039/d5cp03402g

rsc.li/pccp

Silicon (Si)- and tin (Sn)-based materials play a critical role in the green energy sector, with Si being the primary component in solar panels due to its high efficiency and widespread availability. In addition, both Si and Sn are being extensively investigated as high-capacity anode materials in lithium-ion batteries (LIBs), sodium-ion batteries (SIBs), and potassium-ion batteries (KIBs), enhancing energy storage efficiency for sustainable applications. In this work, the potential of utilizing SiN_3 and SnN_3 monolayers as anode materials for KIBs is systematically investigated through first-principles calculations based on density functional theory (DFT). The SiN_3 and SnN_3 monolayers exhibit high cohesive energies of 6.08 and 6.81 eV per atom, respectively. Based on the results of theoretical calculations, both monolayers show excellent mechanical, dynamic, and thermal stability. Furthermore, our computational simulations show that the K-adsorbed AN_3 (A = Si, Sn) systems exhibit metallic properties, leading to excellent electronic conductivity. The diffusion barriers for K ions, as determined by the climbing-image nudged elastic band (CI-NEB) method, are remarkably low: 0.14 eV and 0.27 eV for SiN_3 and SnN_3 monolayers, respectively. Notably, the adsorbed $KSiN_3$ and $KSnN_3$ monolayers offer several stable adsorption sites, leading to high theoretical capacities of 764.43 mAh g^{-1} and 333.47 mAh g^{-1}, respectively. This study significantly advances the design of efficient anode materials for potassium-ion batteries.

1. Introduction

The transition to sustainable energy technologies as an alternative to traditional fossil fuel-based power generation is driven by the global demand for energy.[1] Dependence on fossil fuels has been identified as a major contributor to environmental challenges, including global warming and climate change, leading to a pressing need for more eco-friendly energy solutions.[2] Advances in energy efficiency and significant reductions in overall energy consumption are expected to meet this challenge.[3] To address these challenges, extensive research[4–7] has been undertaken to develop electrochemical systems for transforming and storing energy. Battery technologies are emerging as a promising candidate among the various options and have received considerable attention from both fundamental research and industrial applications.[8–10] Since their first commercialisation in 1991, Li-ion batteries have achieved widespread application in wireless devices like laptops and mobile phones, electric vehicles and different electronic devices.[11–13] However, in promoting sustainable energy development, this energy technology faces problems such as low capacity, poor safety, and depletion of Li resources.[14–16] Sodium- and potassium-ion batteries have recently emerged as promising alternatives to Li-ion battery systems, offering high energy storage, enhanced safety, and lower cost, largely due to the abundant availability of Na and K resources.[17,18] However, KIBs offer notable advantages, including the natural abundance of potassium (K) (2.09 wt% in the earth crust), lower cost, and widespread geographical availability.[19,20] Additionally, potassium-ion batteries have the same operating mechanism as that of lithium-ion batteries.[21] Despite their advantages, sodium (1.02 Å) and potassium (1.38 Å) ions have significantly larger ionic radii compared to lithium ions (0.72 Å), which lead to sluggish ion transport and severe volume changes during cycling.[22] Furthermore, researchers have devoted efforts to developing viable strategies, such as covalent organic frameworks (COFs)[23–25] and metal–organic frameworks (MOFs),[26] to overcome the limitations of LIBs and non-lithium-ion batteries (NLIBs) for further application in next-generation rechargeable batteries. Among various battery components, anode materials are key determinants of the overall efficiency in alkaline battery systems. Graphite has emerged as a widely used material in high-performance LIBs due to its long

---

*Combustion Chemistry Centre, School of Biological and Chemical Sciences, MaREI, Ryan Institute, University of Galway, Galway H91 TK33, Ireland.
E-mail: chongwen.zhou@universityofgalway.ie*

cycle life and high specific surface area. However, its relatively low theoretical capacity (372 mAh g^{-1})[27] and associated safety concerns limit its ability to meet the escalating energy demand. Additionally, graphite's narrow interlayer spacing makes it unsuitable for Na^+ and K^+ ion intercalation, given their large ionic radii,[28] thereby restricting its application in NLIBs. As a result, the development of advanced anode materials tailored for LIBs and NLIBs has garnered increasing attention in recent years.

In recent years, two-dimensional (2D) monolayer materials, with a large surface area that enhances the ion diffusion and insertion processes,[29] have shown exceptional potential as high-performance electrodes.[30,31] Recently, Butt *et al.*[32] and Peng *et al.*[33] investigated the electrochemical performance of the SiN_3 monolayer as a host for Li, Na, Mg, and Ca ion batteries using first-principles calculations. All calculations were carried out using the projector augmented wave (PAW) method within the plane-wave basis set, employing the generalized gradient approximation (GGA) with the Perdew–Burke–Ernzerhof (PBE) functional, and a cutoff energy of 550 eV was applied consistently throughout. The energy barriers and high theoretical capacities for Li, Na, Mg, and Ca are 0.025 eV, 0.034 eV, 0.19 eV, and 0.24 eV, and 1146 mAh g^{-1}, 1146 mAh g^{-1}, 764 mAh g^{-1}, and 764 mAh g^{-1}, respectively. These results indicate that the SiN_3 monolayer possesses excellent theoretical capacities, low energy barriers, and suitable average voltages, demonstrating its potential as an anode material for Li/Na/Mg/Ca ion batteries. Furthermore, the structure and electronic properties of the SiN_3 and SnN_3 monolayers have been thoroughly investigated in previous studies for applications in the fields of photocatalytic hydrolysis and semiconductors, especially in photocatalytic water splitting.[34,35]

Potassium-ion batteries (KIBs) are gaining attention as cost-effective and sustainable alternatives to LIBs due to potassium abundance and similar intercalation chemistry. This study employs first-principles calculations to examine the electrochemical properties of nitrogen-based SiN_3 and SnN_3 monolayers as potential anode materials for KIBs, which remain computationally unexplored. First, we will examine the dynamic and thermal stability of the pristine and K adsorbed SiN_3 and SnN_3 monolayers by the density-functional perturbation theory (DFPT) method and AIMD simulations.[36] In addition, the migration pathways for K atoms on the SiN_3 and SnN_3 monolayers will be investigated by the Cl-NEB method.[37] Finally, the LOBSTER code[38] will be employed to perform crystal orbital Hamilton population (COHP) analysis, providing insights into the interactions between the adsorbed ions and substrate.

2. Computational methods

Density functional theory (DFT) calculations were performed using a plane-augmented wave approach implemented in the Vienna *Ab initio* Simulation Package (VASP).[39,40] For exchange–correlation interactions, the Perdew–Burke–Ernzerhof (PBE) functional was used within the generalised gradient approximation (GGA).[39] The plane-wave cut-off energy was 540 and 520 eV for SiN_3 and SnN_3 monolayers, respectively. The electronic structure was analyzed using both the GGA-PBE approach and the hybrid HSE06 functional.[41] All models employed 2 × 2 × 1 supercells of SiN_3 and SnN_3 with periodic boundary conditions, incorporating a 21 Å vacuum layer setup along the *z*-axis to avoid any interlayer interactions. van der Waals (vdW) interactions were considered using the DFT-D3 approach[42,43] to ensure accurate determination of the adsorption energy strength. A 5 × 5 × 1 Monkhorst–Pack grid with a Gaussian smear width of 0.05 eV was used to sample the Brillouin zone. Adsorption of K at different concentrations on SiN_3 and SnN_3 sheets was used to determine the adsorption energy, voltage profile, capacity, and the amount of charge transfer from K to the sheet by using the Bader charge method. The phonon dispersion was analysed through the DFPT method using the PHONOPY code[44] to assess the dynamic stability. In addition, thermal stability was evaluated by AIMD simulations in the NVT ensemble with a Nosé–Hoover thermostat[36] using a 2 × 2 supercell at 300 K with a 10 000 fs time steps.

The bonding interactions between the adsorbed K atoms and host SiN_3 and SnN_3 monolayers were analysed using the LOBSTER code,[38] and the energy barrier for K atoms across the host surface was analysed using the Cl-NEB method.[45] The following equations were employed to calculate the adsorption energy,[46] average voltage,[47] charge density difference,[48] and cohesive energy:

$$E_{\text{ad}} = \frac{E_{\text{Sub}} - E_{\text{Pristine}} - nE_{\text{K}}}{n} \tag{1}$$

where E_{Sub} denotes the total energy of the K-adsorbed SiN_3 and SnN_3 monolayers and E_{Pristine} represents the total energy of the pristine SiN_3 and SnN_3 monolayers, while E_{K} is the total energy of the bulk K atom, and n is the number of adsorbed K atoms.

$$\Delta\rho = \rho_{\text{Sub}} - \rho_{\text{Pristine}} - \rho_{\text{K}} \tag{2}$$

where ρ_{Sub} and ρ_{Pristine} denote the charge densities of K-adsorbed and pristine SiN_3 and SnN_3 monolayers, respectively, and ρ_{K} is the charge density of an isolated K atom.

$$V_{\text{OCV}} = \frac{E_{\text{Pristine}} - xE_{\text{K}} - E_{\text{Sub}}}{xe} \tag{3}$$

where E_{Pristine} and E_{Sub} represent the total energies of the pristine and K-adsorbed SiN_3 and SnN_3 monolayers and x indicates the number of adsorbed K atoms.

$$E_{\text{coh}} = \frac{E_{\text{Si/Sn}} + 3E_{\text{N}} - E_{\text{SiN}_3/\text{SnN}_3}}{4} \tag{4}$$

where $E_{\text{Si/Sn}}$, E_{N} and $E_{\text{SiN}_3/\text{SnN}_3}$ represent the energies of the Si/Sn atoms, N atoms, and SiN_3 and SnN_3 monolayers, respectively.

3. Results and discussion

3.1. Structural analysis of the pristine and adsorbed systems

The unit cell of SiN_3 and SnN_3 monolayers consists of two silicon and tin atoms and eight nitrogen atoms, and each Si and Sn atom forms bonds with three neighbouring N atoms. The optimised 2 × 2 × 1 supercell structure of the SiN_3 and SnN_3 monolayers is shown in Fig. S1. The obtained optimised lattice parameters are $a = b = 5.06$ Å for SiN_3 and $a = b = 5.25$ Å for SnN_3, which are in line with previous theoretical studies,[32–35] as shown in Table S1. The stability of the pristine SiN_3 and SnN_3 monolayers was confirmed by cohesive energy using eqn (4), which determined the validation of the experimental synthesis of the materials. The calculated cohesive energy for SiN_3 and SnN_3 monolayers is 6.08 eV per atom and 6.87 eV per atom, respectively, which are higher than those of reported 2D monolayers, as shown in Table S2. A higher cohesive energy generally indicates greater ease of materials synthesis.[49] Therefore, the high cohesive energy values support the experimental feasibility of synthesizing the SiN_3 and SnN_3 monolayers. In addition, the bonding nature was examined using the electron localisation function (ELF), as illustrated in Fig. 1(a and b). Typically, ELF values below 0.5 suggest ionic bonding, while a value above 0.5 indicates covalent interactions. A value around 0.5 indicates metallic bonding nature.[49] The ELF plots show electron localisation in the Si–N, N–N, and Sn–N structures, with red/yellow regions depicting strong electron localisation in covalent bonds. To evaluate the dynamic stability of the SiN_3 and SnN_3 monolayers, phonon band dispersion curves were calculated along the high-symmetry paths of the Brillouin zone as shown in Fig. S2. The phonon band structures exhibit no imaginary frequencies throughout the first Brillouin zone, confirming the dynamic stability of the SiN_3 and SnN_3 monolayers. These results align well with previously reported phonon spectra, further validating the structural robustness of both monolayers.[32,35] Additionally, the phonon modes of the SiN_3 and SnN_3 monolayers compare with those of other reported 2D monolayers, as shown in Table S3.

In the present work, we primarily investigate the key properties of the SiN_3 and SnN_3 monolayers with adsorbed K atoms. To evaluate the adsorption rate of the SiN_3 and SnN_3 sheets, it is essential to accurately determine the adsorption position of the K atom on the surface. As shown in Fig. S1(a and b), we select four different sites for adsorption: T1 (top of Si and Sn atoms), H1 (hollow site of the hexagonal Si/Sn_2N_4 ring), H2 (hollow site of the hexagonal N_6 ring), and T2 (top site of N atoms). After optimising the structure, the results shown in Fig. 1(c) indicate that T1 is the most stable adsorption site with the highest adsorption energy. After confirming a stable adsorption site, we also examined the stability, electronic properties, bonding interactions, and the rate of charge transfer at this site. To validate the thermal stability of the batteries during the charging/discharging process, AIMD simulations were performed for $K_{0.125}SiN_3$ and $K_{0.125}SnN_3$ monolayers at 300 K for 10 000 fs, as shown in Fig. 2(a) and (b). After 1000-fs steps of AIMD simulations, the energies of $K_{0.125}SiN_3$ and $K_{0.125}SnN_3$ became stable and fluctuated around equilibrium, while the structural snapshots confirmed stable SiN_3 and SnN_3 frameworks without bond breakage. Furthermore, the elastic constants of the K-adsorbed SiN_3 and SnN_3 monolayers are calculated to determine their mechanical stability. The materials are considered mechanically stable if they meet the Born elastic stability criteria: $C_{11}C_{22} - C_{12} > 0$ and $C_{66} > 0$.[50] Here, C_{11} and C_{22} represent the in-plane stiffness along the x and y directions, respectively, C_{12} is the in-plane coupling constant, and C_{66} corresponds to the shear modulus. The calculated elastic constants are $C_{11} = C_{22} = 113.380$, $C_{12} = C_{21} = 27.560$ and $C_{66} = 42.910$ for the $KSiN_3$ monolayer, and $C_{11} = C_{22} = 53.814$, $C_{12} = C_{21} = 19.035$ and $C_{66} = 17.389$ for the $KSnN_3$ monolayer. These calculated elastic constants for both adsorbed monolayers meet the Born elastic stability criteria, indicating their mechanical robustness. The calculated isotropic in-plane Young's modulus of the adsorbed SiN_3 and SnN_3 monolayers are 106.680 N m^{-1} and 47.080 N m^{-1}, respectively, as illustrated in Fig. 2(c) and (d). A high Young's modulus reflects the structural rigidity and mechanical stability of the material.[51] In comparison, the calculated Young's modulus values of the $K_{0.125}SiN_3$ and $K_{0.125}SnN_3$ monolayers are higher than those of other reported 2D monolayers such as SiP_3 (62.3 N m^{-1}),[52] GeN_3 (94.776 N m^{-1}),[47] SnB (48.58 N m^{-1}),[53] germanene (43.5 N m^{-1}) and stanene (23.5 N m^{-1}).[54] We further use the COHP approach, implemented in the LOBSTER code,[38] to quantify the bonding and antibonding interactions between K and the higher adsorption energy sites of the SiN_3 and SnN_3 monolayers. To evaluate the bonding

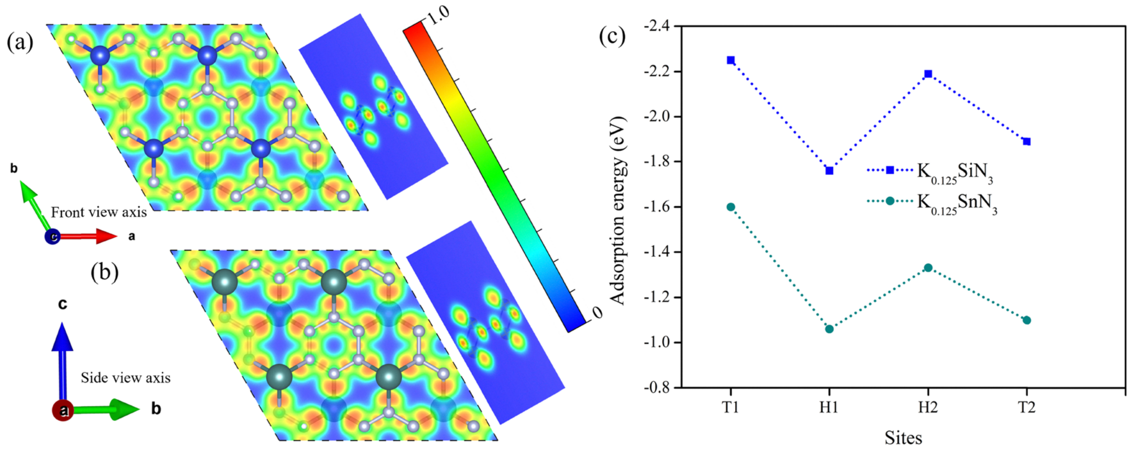

Fig. 1 (a) and (b) Electron localization function maps of the SiN_3 and SnN_3 monolayers. (c) Adsorption energies at different sites.

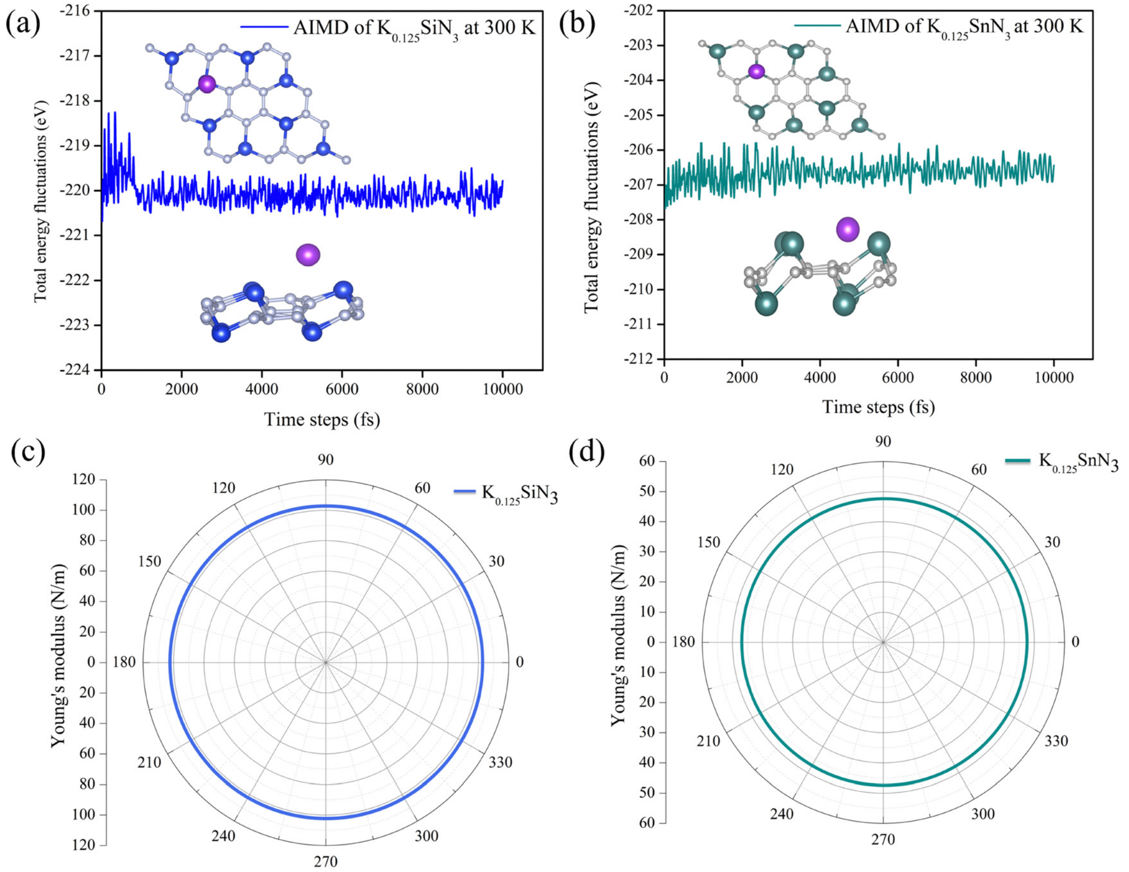

Fig. 2 (a) AIMD simulations of adsorbed $K_{0.125}SiN_3$ and (b) $K_{0.125}SnN_3$ monolayers at 300 K for 10 000 steps with structural snapshots. (c) Young's modulus of $K_{0.125}SiN_3$ and (d) $K_{0.125}SnN_3$ monolayers.

interactions, COHP analysis was performed for the K–Si and K–Sn bonds with bond lengths of 4.02489 Å and 3.55485 Å, respectively, as shown in Fig. 3(a) and (b). A negative value in the COHP diagram indicates a bonding interaction, while a positive value signifies an antibonding contribution.[55] The integrated crystal orbital Hamilton population (ICOHP), calculated up to the Fermi level, provides an effective metric for bond strength. According to the principle that a more negative, dimensionless ICOHP value, correspond to stronger bonding and enhanced chemical stability.[56] The calculated ICOHP values for K–Si and K–Sn bonds are −0.1022 and −0.15401, suggesting a stronger bonding interaction in K–Sn compared to K–Si.

The charge density differences between K and the host SiN_3 and SnN_3 monolayers were calculated using eqn (2), and the results are shown in Fig. 3(c) and (d). The yellow regions represent electron accumulation zones (electron acceptor region), while cyan regions indicate electron depletion zones, where electrons transfer from K to the SiN_3 and SnN_3 monolayers. Furthermore, based on the Bader charge analysis, we calculated the quantity of charge transfer. We calculated the amount of charge transfer from K atoms to the SiN_3 and SnN_3 monolayers to be 0.84 e^- and 0.69 e^-, respectively. This suggests that K undergoes significant polarization upon interacting with the surface of the SiN_3 and SnN_3 monolayers.

3.2. Theoretical capacity and voltage profile analysis with top/bottom K adsorption

With increasing K adsorption on the surface of the SiN_3 and SnN_3 monolayers, the adsorption energy decreases due to the increase of Coulomb's interactions between potassium ions (K^+–K^+). To minimize these Coulombic repulsive forces, we selected top and bottom adsorption sites on the surfaces of the SiN_3 and SnN_3 monolayers. As T1 is the most favourable site for adsorption, we initiated our study by gradually populating the T1 sites on the top surface of the SiN_3 and SnN_3 monolayers with K atoms. Subsequently, we increased the K content by occupying the four corresponding T1 sites on the bottom side, yielding the concentration ratio of $x = 1$, and forming a complete K layer on both the top and bottom surfaces. In the second phase, we adsorbed more K atoms with a concentration ratio (x) of 2, forming the second layer. As shown in Fig. 4(a), the adsorption interactions between K atoms and the host are still negative. As a result, K_2SiN_3 and K_2SnN_3 monolayers exhibit the highest possible K concentrations, where the surface of both monolayers is fully covered by two layers of K ions, as shown in Fig. S3 and S4. The variation in lattice expansion at the highest K content is 0.14% and 1.42% for the SiN_3 and SnN_3 monolayers, respectively. Notably, the volume change upon adsorption/desorption of K atoms on the SiN_3 and SnN_3 monolayers is smaller than the value during the lithiation/

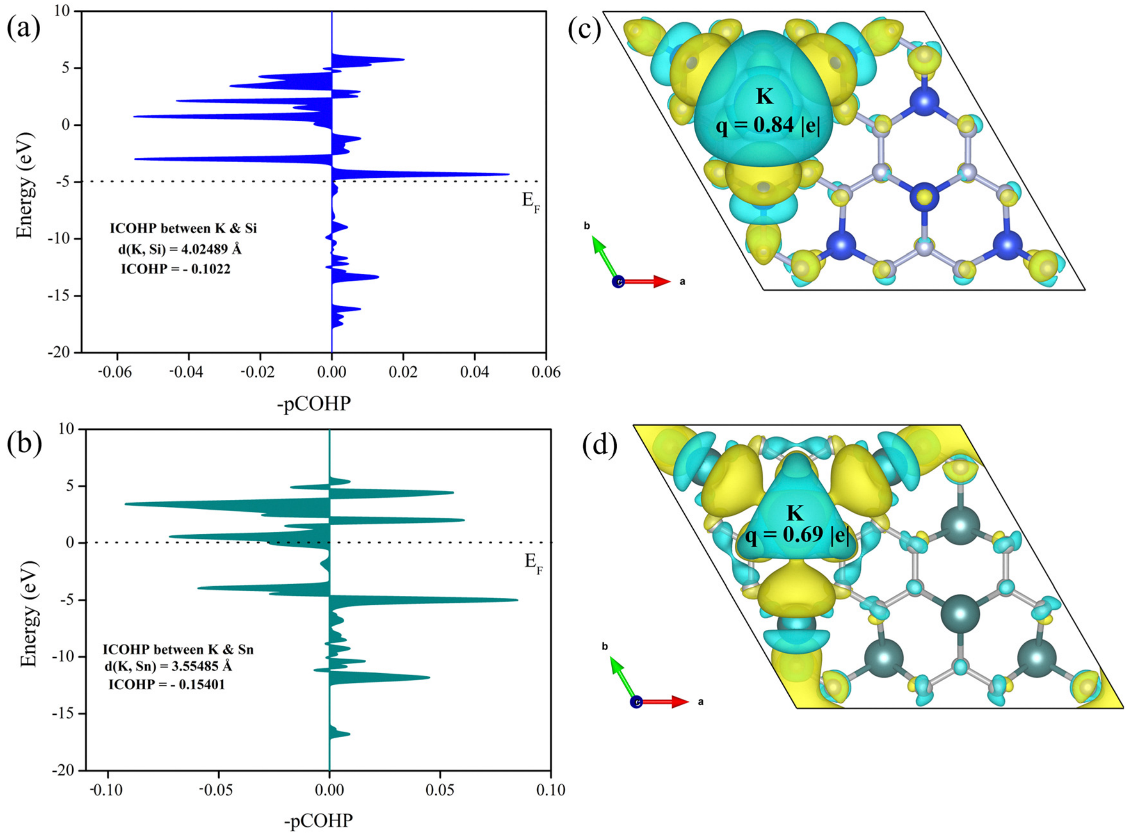

Fig. 3 Crystal orbital Hamilton population (COHP) analysis of interactions between (a) K and Si atoms and (b) K and Sn atoms; (c)–(d) charge density differences and the corresponding charge transfer for the T1–$K_{0.125}SiN_3$ and T1–$K_{0.125}SnN_3$ monolayers.

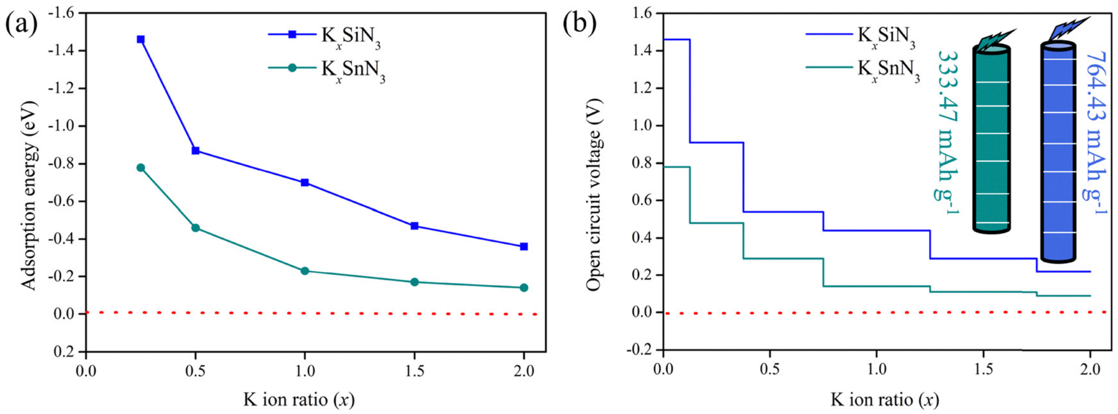

Fig. 4 (a) Top/bottom adsorption energies of the SiN_3 and SnN_3 monolayers at different K-ion ratios. (b) Voltage profile and maximum theoretical storage capacity.

delithiation process in graphite (10%),[57] indicating that expansion and contraction in the SiN_3 and SnN_3 monolayers are not a concern.[58] The slight lattice variation observed indicates that the SiN_3 and SnN_3 monolayers maintain structural integrity during intercalation and deintercalation of metal atoms, highlighting their robustness and suitability for stable cycling performance.

Furthermore, the performance of rechargeable metal-ion batteries is highly dependent on their storage capacity and open circuit voltage (OCV), which are analysed using the charge–discharge cycles of the cell. Thus, the anode reaction during the potassiation and depotassiation processes can be explained by the following relations:

$$SiN_3 + xK^+ + xe^- \leftrightarrow K_xSiN_3 \quad (5)$$

$$SnN_3 + xK^+ + xe^- \leftrightarrow K_xSnN_3 \quad (6)$$

These reactions initiate the flow of electrons through the external circuit, while ions such as K^+ continue to move between

Table 1 Comparative study of the SiN_3 and SnN_3 monolayers with previously reported 2D materials for battery applications

Materials	Energy barrier (eV)	TSE (mAh g^{-1})	Ref.
$KSiN_3$	0.14	764.43	This work
$KSnN_3$	0.29	333.47	This work
$MgSiN_3$	0.19	764	33
$CaSiN_3$	0.24	764	33
KSnB	0.07	517.44	53
KTiSe	0.33	422.63	51
$NaSnP_3$	0.03	253.31	63
$LiSbP_3$	0.44	499.36	64
KSnO	0.07	398	65
$KMoS_2$	0.063	334	66
$KSnSe_2$	0.10	387	46
$KTiS_2$	0.44	282	67
KSnS	0.14	355	21
KSnSe	0.16	271	21
KTi_3C_2	0.10	191.8	68
$KTNiSe_2$	0.05	247	69

the electrolytes and the electrodes during charging/discharging of the battery. The trend of OCV profiles with increasing K content on the K_xSiN_3 and K_xSnN_3 monolayers as shown in Fig. 4(b). For $KSiN_3$, the OCV decreased from 1.4 V to 0.22 V, while for $KSnN_3$, it dropped from 0.78 V to 0.090 V. The decreasing trend in OCV is due to the decrease of adsorption energy with increasing K concentration. The average voltage is calculated to be 0.48 V and 0.22 V for SiN_3 and SnN_3 monolayers, respectively, by taking the mean value over the entire range, which falls within the ideal range of 0.1–1.0 V for KIB anode materials.[59,60] This downshift of OCV in SiN_3 and SnN_3 monolayers could ensure safety and rate performance in practical applications. Furthermore, the theoretical capacity of the K_xSiN_3 and K_xSnN_3 monolayers is determined by using the formula: $C = \dfrac{x_{\max}F}{M_{SiN_3/SnN_3}}$,[61] where F is the Faraday constant (26 801 mAh mol^{-1}), M_{Si/SnN_3} is the molar mass per formula unit of the SiN_3 and SnN_3 monolayers, and $x_{\max}$ represents the highest possible amount of K loaded onto the SiN_3 and SnN_3 monolayers. The calculated theoretical storage capacity of the SiN_3 and SnN_3 monolayers is 764.43 mAh g^{-1} and 333.47 mAh g^{-1}, respectively, which is higher than or comparable to those of other 2D materials, as shown in Table 1.

In addition, to better understand the mechanism of K-ion adsorption on the SiN_3 and SnN_3 monolayers, the electron localization function (ELF) map along the (100) plane for K_xSiN_3 and K_xSnN_3 monolayers (x = 1, 2) is shown in Fig. S5. As the concentration of K increases, some of the valence electrons are transferred from K atoms to the SiN_3 and SnN_3 surfaces, forming an electron-rich region around the K atoms. This accumulation of excess electrons facilitates multilayer adsorption. At high K atom adsorption concentration (x = 2), negatively charged electron clouds were evenly distributed around the K^+ ions. These electron clouds contributed to stabilizing the adsorption layer by enabling electrostatic attraction and reducing repulsive interactions between K^+ atoms.[62]

3.3. Electronic conductivity and rate performance of K-ion batteries

The conductivity and mobility of the metal ions on the electrode surface are critical parameters in the charging and discharging processes and have a major impact on battery performance. Higher electronic conductivity may reduce the risk of overheating of the electrode material.[46,65] Here, we calculate the electronic band structure and partial density of states (PDOS) with GGA-PBE, as shown Fig. S6, and the hybrid HSE06 functional as shown in Fig. 5. As shown in Fig. 5(a) and (b), the pristine SiN_3 and SnN_3 monolayers exhibit semiconducting nature. After K adsorption, the $KSiN_3$ and $KSnN_3$ monolayers display metallic characteristics, as shown in Fig. 5(c) and (d), indicating enhanced electronic conductivity compared with the undoped SiN_3 and SnN_3 monolayers. Furthermore, the projected density of states (PDOS) of the $KSiN_3$ and $KSnN_3$ monolayers reveals that the states near the Fermi level are predominantly composed of Si_s, Sn_s, Si_p, Sn_p, and K_s orbitals, as shown Fig. S7. The presence of these orbitals near the Fermi level indicates a significant contribution to the electronic conduction. Such orbital interactions suggest strong hybridization between the adsorbed potassium atoms and the host monolayers, facilitating enhanced charge delocalization. This hybridization leads to a higher density of conducting states, thereby improving the intrinsic electrical conductivity of the system. Compared to the pristine SiN_3 and SnN_3 monolayers, the increased density of states near the Fermi level suggests electron transfer from the K atom to the host SiN_3 and SnN_3 monolayers. Furthermore, we consider the path for K ion transport on the surface of the SiN_3 and SnN_3 monolayers, as shown in Fig. 6. These ions transported within the electrode play a key role in determining the rate performance of the system. Improved battery charge/discharge performance is achieved by a low diffusion energy barrier, which allows faster ion transport. For diffusion of K, we use the Cl-NEB method,[37] which identified two states: the initial state (low energy state) and the final state (high energy state). The minimum on the diffusion path corresponds to the most stable position (or local equilibrium position) of the diffusion atom or ion. Physically, this represents the site where the atom experiences the lowest potential energy and is most likely to reside prior to migrating to an adjacent site. The energy difference between this minimum state and the adjacent saddle point (transition state) along the path identified the energy barrier. This provides insight into how efficient the charges are in the charging and discharging processes in batteries. Due to the symmetric lattice structures of the SiN_3 and SnN_3 monolayers, a typical K-ion diffusion pathway (T1–H2–T1) is investigated. In this pathway, K ions migrate from the top of a Si/Sn atom (T1), pass through the hollow site (H2), and reach a neighbouring T1 site. The calculated energy barriers along this pathway are 0.14 eV for SiN_3 and 0.29 eV for SnN_3. In contrast, the corresponding energy barriers for Li and Na ions along the same pathway are 0.29 eV and 0.49 eV,[32] while those for Mg and Ca are 0.22 eV and 0.28 eV,[33] respectively. Compared with other reported 2D materials, as summarized in Table 1, the SiN_3 and SnN_3 monolayers exhibit significantly lower diffusion barriers for K-ions, indicating faster ion transport and potentially higher charge and discharge rates. As a result, the enhanced electronic conductivity and lower ion diffusion barriers suggest that the SiN_3 and SnN_3 monolayers are promising host materials for potassium-ion batteries (KIBs).

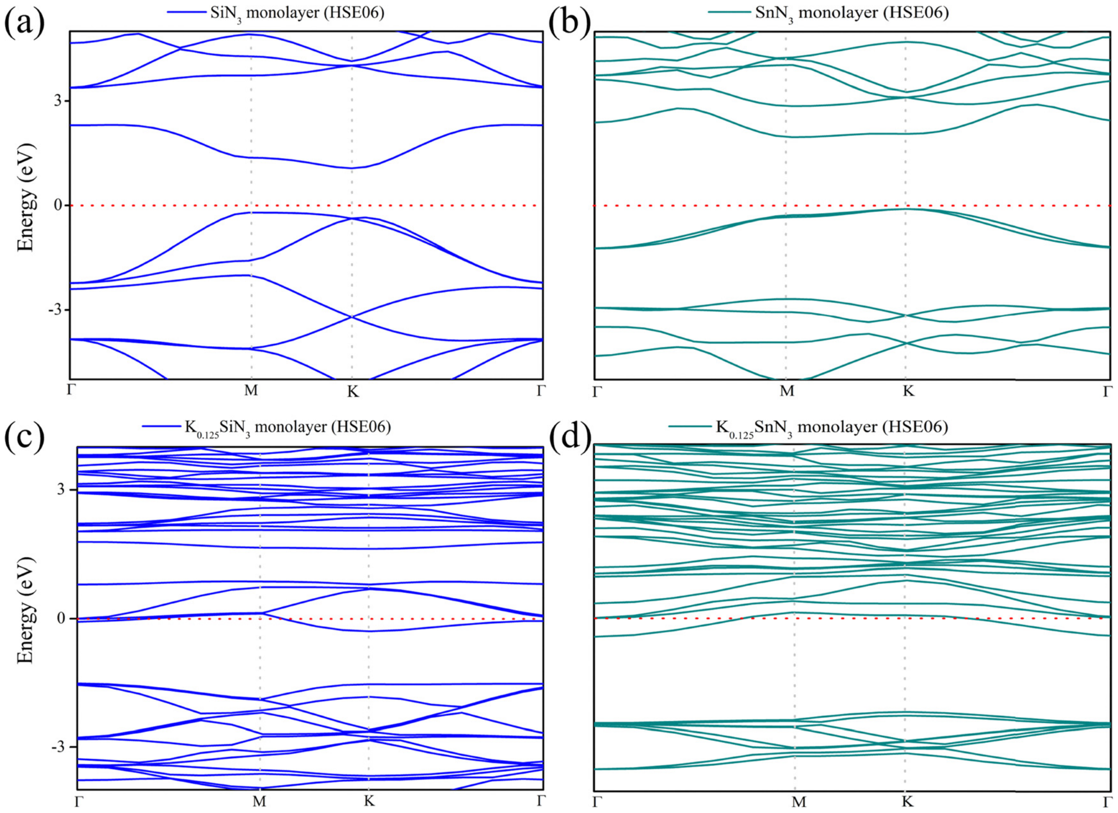

Fig. 5 Electronic band structures of the pristine (a) SiN_3 and (b) SnN_3 monolayers, and K-adsorbed (c) $K_{0.125}SiN_3$ and (d) $K_{0.125}SnN_3$ monolayers, calculated using the hybrid HSE06 functional.

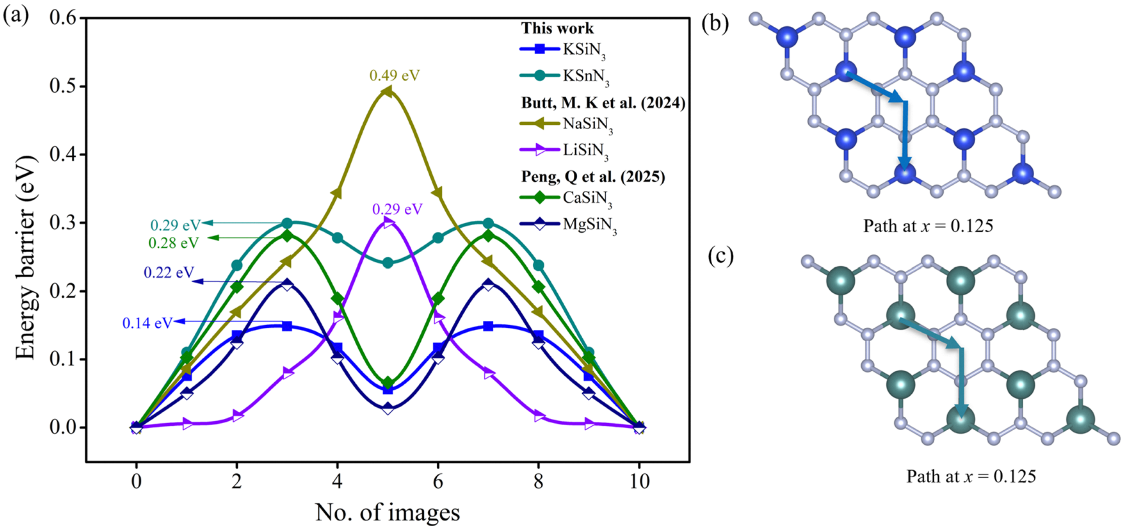

Fig. 6 (a)–(c) The minimum energy barriers of the $KSiN_3$ and $KSnN_3$ monolayers with the corresponding paths compared with previously reported data.[32,33]

4. Conclusions

In summary, first-principles calculations were conducted to assess the potential of nitrogen-rich SiN_3 and SnN_3 monolayers for applications in potassium-ion batteries (KIBs). Our results show that the K ion is stably adsorbed onto the T1–SiN_3 and T1–SnN_3 sites with high adsorption energies, strong bonding interactions, and high charge transfer rates. The addition of K-ions into the system induces a shift from semiconducting to metallic nature, significantly enhancing the material's electronic conductivity. The adsorbed SiN_3 and SnN_3 monolayers are mechanically stable according to the calculated elastic constants and Young's modulus. The minimum volume expansion of fully adsorbed SiN_3 and SnN_3 monolayers is smaller than that of commercial anode materials, indicating that intercalation and deintercalation of metal atoms are not a concern. In addition, both fully adsorbed K_2SiN_3 and K_2SnN_3 monolayers yield high theoretical capacities of 764.43 and 333.47 mAh g^{-1} and low average open-circuit voltages of 0.48 V and 0.22 V, respectively. The $KSiN_3$ and $KSnN_3$ monolayers exhibit low migration energy barriers of 0.14 eV and 0.27 eV, respectively, which greatly facilitate ionic mobility and enhance the charging and discharging processes. The computational results indicate that AN_3 (A = Si, Sn) monolayers have strong potential as anode materials for KIBs.

Conflicts of interest

The authors declare that they have no known competing financial interests or personal relationships that could have appeared to influence the work reported in this paper.

Data availability

The data supporting the findings of this study are available within the article and its supplementary information. The supplementary information includes optimized geometries, phonon band spectra, electron localization function (ELF) plots at different concentrations, electronic band structures, and density of states (DOS). Additional supporting information can be accessed at **https://doi.org/10.1039/d5cp03402g**.

Acknowledgements

The authors would like to acknowledge the support from the School of Biological and Chemical Sciences at the University of Galway, Ireland. In addition, they would like to extend their gratitude to the Irish Centre for High End Computing (ICHEC) for providing the computational resources.

References

1 F. Rizzi, N. J. van Eck and M. Frey, *Renewable Energy*, 2014, **62**, 657–671.
2 E. Vine, *Energy Effic.*, 2008, **1**, 49–63.
3 S. Sorrell, *Renewable Sustainable Energy Rev.*, 2015, **47**, 74–82.
4 H. D. Yoo, E. Markevich, G. Salitra, D. Sharon and D. Aurbach, *Mater. Today*, 2014, **17**, 110–121.
5 T. Kopac, *Atomically Precise Electrocatalysts for Electrochemical Energy Applications*, Springer, 2024, pp. 71–91.
6 R. Sharma, H. Kumar, G. Kumar, S. Sharma, R. Aneja, A. K. Sharma, R. Kumar and P. Kumar, *Chem. Eng. J.*, 2023, **468**, 143706.
7 A. Olabi, K. Elsaid, K. Obaideen, M. A. Abdelkareem, H. Rezk, T. Wilberforce, H. M. Maghrabie and E. T. Sayed, *Int. J. Thermofluids*, 2023, **20**, 100498.
8 J. Ma, Y. Li, N. S. Grundish, J. B. Goodenough, Y. Chen, L. Guo, Z. Peng, X. Qi, F. Yang and L. Qie, *J. Phys. D: Appl. Phys.*, 2021, **54**, 183001.
9 E. Fan, L. Li, Z. Wang, J. Lin, Y. Huang, Y. Yao, R. Chen and F. Wu, *Chem. Rev.*, 2020, **120**, 7020–7063.
10 G. L. Soloveichik, *Annu. Rev. Chem. Biomol. Eng.*, 2011, **2**, 503–527.
11 S. Megahed and W. Ebner, *J. Power Sources*, 1995, **54**, 155–162.
12 B. Kennedy, D. Patterson and S. Camilleri, *J. Power Sources*, 2000, **90**, 156–162.
13 K. Zaghib, A. Guerfi, P. Hovington, A. Vijh, M. Trudeau, A. Mauger, J. Goodenough and C. Julien, *J. Power Sources*, 2013, **232**, 357–369.
14 C. Li, L. He, X. Li, J. Luo, X. Zhu, Z. Chen and M. Xu, *J. Mater. Chem. C*, 2021, **9**, 6802–6814.
15 A. Farmann, W. Waag, A. Marongiu and D. U. Sauer, *J. Power Sources*, 2015, **281**, 114–130.
16 T. Ould Ely, D. Kamzabek and D. Chakraborty, *Front. Energy Res.*, 2019, **7**, 71.
17 V. Palomares, P. Serras, I. Villaluenga, K. B. Hueso, J. Carretero-González and T. Rojo, *Energy Environ. Sci.*, 2012, **5**, 5884–5901.
18 S. Komaba, T. Hasegawa, M. Dahbi and K. Kubota, *Electrochem. Commun.*, 2015, **60**, 172–175.
19 I. Sultana, M. M. Rahman, Y. Chen and A. M. Glushenkov, *Adv. Funct. Mater.*, 2018, **28**, 1703857.
20 X. Zou, P. Xiong, J. Zhao, J. Hu, Z. Liu and Y. Xu, *Phys. Chem. Chem. Phys.*, 2017, **19**, 26495–26506.
21 Q. Peng, J. Rehman, M. K. Butt, S. A. Shafiee, Z. Yang, M. Ouladsmane, J. Liu, M. Ullah and Z. Li, *J. Phys. Chem. C*, 2023, **127**, 15730–15737.
22 Y. Sun, F. Zeng, Y. Zhu, P. Lu and D. Yang, *J. Energy Chem.*, 2021, **61**, 531–552.
23 D. Zhu, G. Xu, M. Barnes, Y. Li, C. P. Tseng, Z. Zhang, J. J. Zhang, Y. Zhu, S. Khalil and M. M. Rahman, *Adv. Funct. Mater.*, 2021, **31**, 2100505.
24 B. Ball and P. Sarkar, *J. Phys. Chem. C*, 2020, **124**, 15870–15878.
25 P. Das, B. Ball and P. Sarkar, *Phys. Chem. Chem. Phys.*, 2022, **24**, 21729–21739.
26 X. Gao, Y. Dong, S. Li, J. Zhou, L. Wang and B. Wang, *Electrochem. Energy Rev.*, 2020, **3**, 81–126.
27 H. Zhang, Y. Yang, D. Ren, L. Wang and X. He, *Energy Storage Mater.*, 2021, **36**, 147–170.
28 K. Song, C. Liu, L. Mi, S. Chou, W. Chen and C. Shen, *Small*, 2021, **17**, 1903194.
29 C. Tan, X. Cao, X.-J. Wu, Q. He, J. Yang, X. Zhang, J. Chen, W. Zhao, S. Han and G.-H. Nam, *Chem. Rev.*, 2017, **117**, 6225–6331.
30 R. Tian, M. Breshears, D. V. Horvath and J. N. Coleman, *ACS Nano*, 2020, **14**, 3129–3140.
31 J. Du, H. Lin and Y. Huang, *Mater. Sci. Semicond. Process.*, 2024, **172**, 108086.
32 M. K. Butt, J. Rehman, Z. Yang, A. El-marghany, Z. Li and M. F. Shibl, *J. Energy Storage*, 2024, **93**, 112290.
33 Q. Peng, J. Rehman, M. K. Butt, L. Tao, U. Younis, A. El-marghany, M. B. Hanif and Z. Li, *Mater. Today Chem.*, 2025, **43**, 102465.

34 N. Zhang, Y. Shen, L. Lv, X. Meng, Y. Zhang, X. Yang, M. Zhou, K. Wang, Q. He and B. Zhang, *Vacuum*, 2024, **219**, 112711.
35 S. Wu, Y. Shen, X. Gao, Y. Ma and Z. Zhou, *Nanoscale*, 2019, **11**, 18628–18639.
36 G. J. Martyna, M. L. Klein and M. Tuckerman, *J. Chem. Phys.*, 1992, **97**, 2635–2643.
37 D. Sheppard, R. Terrell and G. Henkelman, *J. Chem. Phys.*, 2008, **128**, 134106.
38 S. Maintz, V. L. Deringer, A. L. Tchougréeff and R. Dronskowski, *J. Comput. Chem.*, 2016, 1030–1035.
39 J. P. Perdew, K. Burke and M. Ernzerhof, *Phys. Rev. Lett.*, 1996, **77**, 3865.
40 P. E. Blöchl, *Phys. Rev. B: Condens. Matter Mater. Phys.*, 1994, **50**, 17953.
41 J. Heyd, G. E. Scuseria and M. Ernzerhof, *J. Chem. Phys.*, 2003, **118**, 8207–8215.
42 S. Grimme, J. Antony, S. Ehrlich and H. Krieg, *J. Chem. Phys.*, 2010, **132**, 154104.
43 Y.-S. Lin, G.-D. Li, S.-P. Mao and J.-D. Chai, *J. Chem. Theory Comput.*, 2013, **9**, 263–272.
44 A. Togo and I. Tanaka, *Scr. Mater.*, 2015, **108**, 1–5.
45 G. Henkelman, B. P. Uberuaga and H. Jónsson, *J. Chem. Phys.*, 2000, **113**, 9901–9904.
46 J. Rehman, X. Fan, M. Butt, A. Laref, V. A. Dinh and W. Zheng, *Appl. Surf. Sci.*, 2021, **566**, 150522.
47 L. Ali, J. Rehman and C.-W. Zhou, *J. Phys. Chem. Solids*, 2025, 112940.
48 J. Rehman, X. Fan and W. Zheng, *Appl. Surf. Sci.*, 2019, **496**, 143625.
49 Q. Peng, J. Rehman, M. K. Butt, D. Wang, L. Tao, A. M. Tighezza and J. Dai, *J. Energy Storage*, 2024, **95**, 112591.
50 F. Mouhat and F.-X. Coudert, *Phys. Rev. B: Condens. Matter Mater. Phys.*, 2014, **90**, 224104.
51 M. Wang, S. Wang, Y. Liang, Y. Xie, X. Ye and S. Sun, *Phys. Chem. Chem. Phys.*, 2023, **25**, 24625–24635.
52 Y. Kuai, C. Chen, S. Gao, W. Chen, J. Hao, G. Wu, F. Chen, S. Guo, L. Wu and P. Lu, *Appl. Surf. Sci.*, 2022, **586**, 152510.
53 Y. Kuai, C. Chen, E. Abduryim, S. Gao, W. Chen, G. Wu, L. Wu, C. Dong, W. Zou and P. Lu, *Phys. Chem. Chem. Phys.*, 2022, **24**, 23737–23748.
54 B. Peng, D. Zhang, H. Zhang, H. Shao, G. Ni, Y. Zhu and H. Zhu, *Nanoscale*, 2017, **9**, 7397–7407.
55 H. Rghioui, M. S. Zyane, H. R. Jappor, M. Diani, A. Marjaoui and M. Zanouni, *J. Phys. Chem. Solids*, 2025, **201**, 112660.
56 Y. Lin, X. Zhou and W. Chen, *Solid State Commun.*, 2025, 116018.
57 J. Vetter, P. Novák, M. R. Wagner, C. Veit, K.-C. Möller, J. Besenhard, M. Winter, M. Wohlfahrt-Mehrens, C. Vogler and A. Hammouche, *J. Power Sources*, 2005, **147**, 269–281.
58 X. Lv, F. Li, J. Gong, J. Gu, S. Lin and Z. Chen, *Phys. Chem. Chem. Phys.*, 2020, **22**, 8902–8912.
59 P. Xiang, X. Chen, B. Xiao and Z. M. Wang, *ACS Appl. Mater. Interfaces*, 2019, **11**, 8115–8125.
60 D. Çakır, C. Sevik, O. Gülseren and F. M. Peeters, *J. Mater. Chem. A*, 2016, **4**, 6029–6035.
61 M. K. Butt, J. Rehman, Z. Yang, S. Wang, A. El-Zatahry, A. S. Alofi, M. D. Albaqami, R. G. Alotabi, A. Laref and K. Jin, *Phys. Chem. Chem. Phys.*, 2022, **24**, 29609–29615.
62 S. Xu, X. Fan, J. Liu, Q. Jiang, W. Zheng and D. J. Singh, *Electrochim. Acta*, 2019, **297**, 497–503.
63 C.-S. Liu, X.-L. Yang, J. Liu and X.-J. Ye, *ACS Appl. Energy Mater.*, 2018, **1**, 3850–3859.
64 H. Rghioui, M. S. Zyane, H. Ghannam, M. A. Tamerd, M. Diani, M. Zanouni and A. Marjaoui, *Chem. Phys. Lett.*, 2024, 141429.
65 Q. Peng, J. Rehman, M. K. Butt, Z. Yang, S. Wang, E. A. Al-Ammar, M. Sillanpää, V. A. Dinh and M. F. Shibl, *J. Mater. Sci.*, 2023, **58**, 3208–3218.
66 J. Rehman, X. Fan, A. Laref, V. A. Dinh and W. Zheng, *J. Alloys Compd.*, 2021, **865**, 158782.
67 Z. Zhang, M. Yang, N. Zhao, L. Wang and Y. Li, *Phys. Chem. Chem. Phys.*, 2019, **21**, 23441–23446.
68 D. Er, J. Li, M. Naguib, Y. Gogotsi and V. B. Shenoy, *ACS Appl. Mater. Interfaces*, 2014, **6**, 11173–11179.
69 Y. Shen, J. Liu, X. Li and Q. Wang, *ACS Appl. Mater. Interfaces*, 2019, **11**, 35661–35666.